nature materials

LETTERS

PUBLISHED ONLINE: 9 MARCH 2015 | DOI: 10.1038/NMAT4232

Origami structures with a critical transition to bistability arising from hidden degrees of freedom

Jesse L. Silverberg[1]*, Jun-Hee Na[2], Arthur A. Evans[3], Bin Liu[1], Thomas C. Hull[4], Christian D. Santangelo[3], Robert J. Lang[5], Ryan C. Hayward[2] and Itai Cohen[1]

Origami is used beyond purely aesthetic pursuits to design responsive and customizable mechanical metamaterials[1–8]. However, a generalized physical understanding of origami remains elusive, owing to the challenge of determining whether local kinematic constraints are globally compatible and to an incomplete understanding of how the folded sheet's material properties contribute to the overall mechanical response[9–14]. Here, we show that the traditional square twist, whose crease pattern has zero degrees of freedom (DOF) and therefore should not be foldable, can nevertheless be folded by accessing bending deformations that are not explicit in the crease pattern. These hidden bending DOF are separated from the crease DOF by an energy gap that gives rise to a geometrically driven critical bifurcation between mono- and bistability. Noting its potential utility for fabricating mechanical switches, we use a temperature-responsive polymer-gel version of the square twist to demonstrate hysteretic folding dynamics at the sub-millimetre scale.

A key theme unifying the study of biopolymer gels[15,16], biological tissues[17], kinematic mechanisms[18–21], granular media[22–24], network glasses[25] and architectural elements[26] is the competition between the number of internal DOF, N_f, and the number of internal mechanical constraints, N_c. The macroscopic behaviour of these systems in the absence of self-stresses[27,28] is said to be underconstrained when $N_f > N_c$, overconstrained when $N_f < N_c$, and isostatic, or marginally stable, when $N_f = N_c$. This framework, which was initially laid out by J. C. Maxwell in 1864, has been instrumental in understanding a diverse range of mechanical phenomena in constraint-based materials, including rigidity percolation[16], topologically protected zero energy modes[19], nonlinear elasticity[16] and shock waves[24]. A feature intrinsic to real physical materials but often left out of simpler models is the existence of a hierarchy of DOF, each with its own associated energy scale. When the details of these internal features are incorporated, systems can be overconstrained and rigid with respect to low-energy loading, but underconstrained and compliant as higher-energy DOF are accessed. Thus, N_f should be thought of as a variable quantity that changes with the experimental energy scale.

Although these observations are fairly general, the emergent mechanical phenomena that can be found in materials as the DOF hierarchy is probed has not been well examined. Indeed, this problem plays out in origami mechanics, where crease patterns that are mathematically unfoldable because $N_f \leq N_c$ nevertheless easily fold when made by hand[10,11,29,30]. In essence, the discrepancy originates when origami structures are modelled as a series of rigid polyhedra connected by freely rotating torsional hinges. Although rigid foldability appears to be a reasonable simplification for the folding behaviour, the fact that real materials can bend is a critical piece of missing phenomenology. In fact, there is at present no general approach for understanding and predicting the mechanical behaviour of origami structures when their material properties are taken into account. Although numerous examples of unfoldable crease patterns exist, we here investigate the mechanics of a single unit from the square-twist origami tessellation[1] (Fig. 1a,b; see also Supplementary Movies 1 and 2 and Supplementary Fig. 1). Even in this simple test case, we find a rich set of mechanical behaviours that illuminate general principles applicable to any material with measurably different energy scales separating overconstrained and underconstrained states.

The square-twist pattern consists of alternating square and rhombus facets, characterized by the length L and plane angle ϕ, in which the internal edges are either all mountain or valley creases. An analysis of the geometric constraints reveals the pattern is isostatic. Essentially, this arises from the four-fold rotational symmetry of the structure, which imposes a cyclic set of constraints on the four creases that define the central square facet (Supplementary Information). Although this observation indicates that the crease pattern should not be foldable, a trigonometric analysis of the normalized edge-to-edge distance x/L shows that the square twist allows two isolated states corresponding to the fully unfolded and folded configurations (Fig. 1c, upper and lower black lines, respectively, and Supplementary Fig. 2).

Experiments measuring x/L on folded paper sheets without external loading (Methods; Fig. 1c, red data points) indicate qualitatively different behaviour than the crease geometry's naive prediction of rigidity. Instead, below a critical plane angle $\phi_c = (25 \pm 2.5)^\circ$, the distinction between folded and unfolded configurations is not observed; the structure is monostable with an intermediate value of x/L (for example, Fig. 1b, side views). Above ϕ_c, both folded and unfolded configurations are observed; the folded configuration exhibits x/L values that nearly match the prediction, whereas the unfolded configuration exhibits x/L values that are smaller than predicted for ideal sheets (Fig. 1b, side view, and Fig. 1c). Although the crease pattern does not admit solutions between folded and unfolded branches for any $\phi > 0^\circ$, direct observations during the folding process reveal that the facets bend by a finite amount rather than remaining flat. These deformations are additional DOF hidden from the bare crease pattern, and are essential for foldability as they enable the structure to access otherwise geometrically forbidden configurations. It is the combination of this facet bending and the non-zero rest angles of the creases, which are plastically set when the sheet is fully folded, that gives rise to the observed intermediate configurations.

[1]Physics Department, Cornell University, Ithaca, New York 14853, USA. [2]Department of Polymer Science and Engineering, University of Massachusetts, Amherst, Massachusetts 01003, USA. [3]Department of Physics, University of Massachusetts, Amherst, Massachusetts 01003, USA. [4]Department of Mathematics, Western New England University, Springfield, Massachusetts 01119, USA. [5]Lang Origami, Alamo, California 94507, USA.
*e-mail: JLS533@cornell.edu

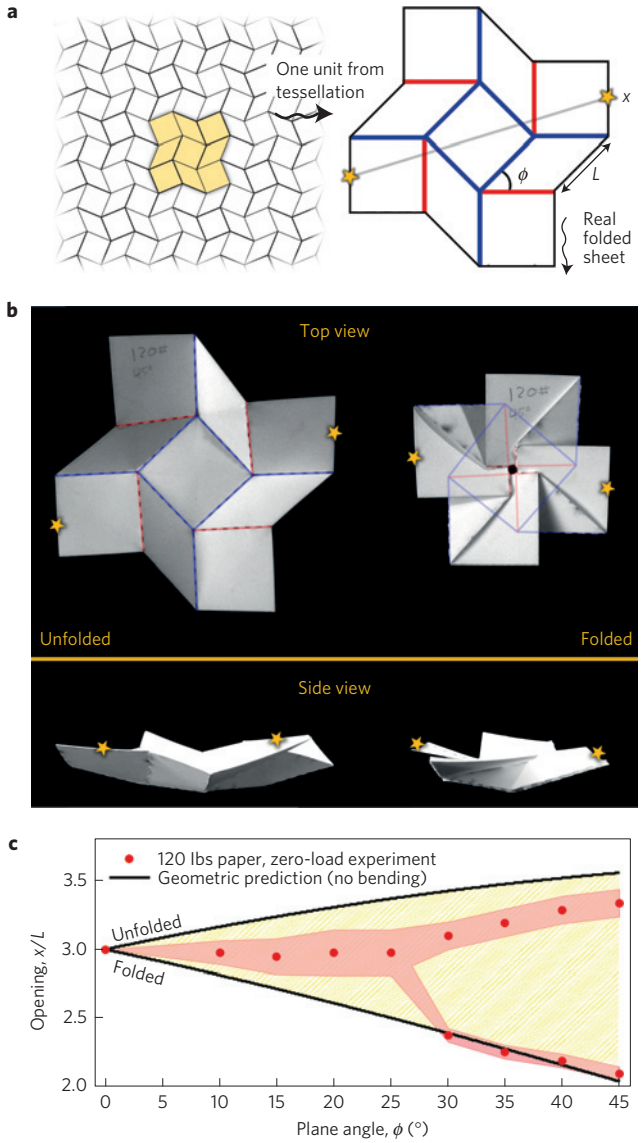

Figure 1 | Schematics and photographs introducing the square twist's essential geometric properties and mechanical characteristics. a, The square-twist folding pattern is shown with the edges in black, mountain creases in red, and valley creases in blue. The geometry is defined by the length, L, and the plane angle, ϕ. The Euclidean distance, x, between the two yellow stars quantifies the macroscopic configuration between folded and unfolded states. **b**, Photographs of a square twist with $\phi = 45°$ illustrate out-of-plane deformations, and the stars define x when the square twist is unfolded and folded. **c**, Comparison of geometric predictions to experimental measurements for x/L as a function of ϕ based purely on the crease pattern reveals qualitative disagreement. The former has bistable solutions for all non-zero ϕ corresponding to folded and unfolded configurations (black lines), and no permissible configurations between these two states (lightly shaded region between lines). Experimental measurements, however, exhibit regions with mono- and bistable solutions depending on ϕ (red points, errors are shaded bands).

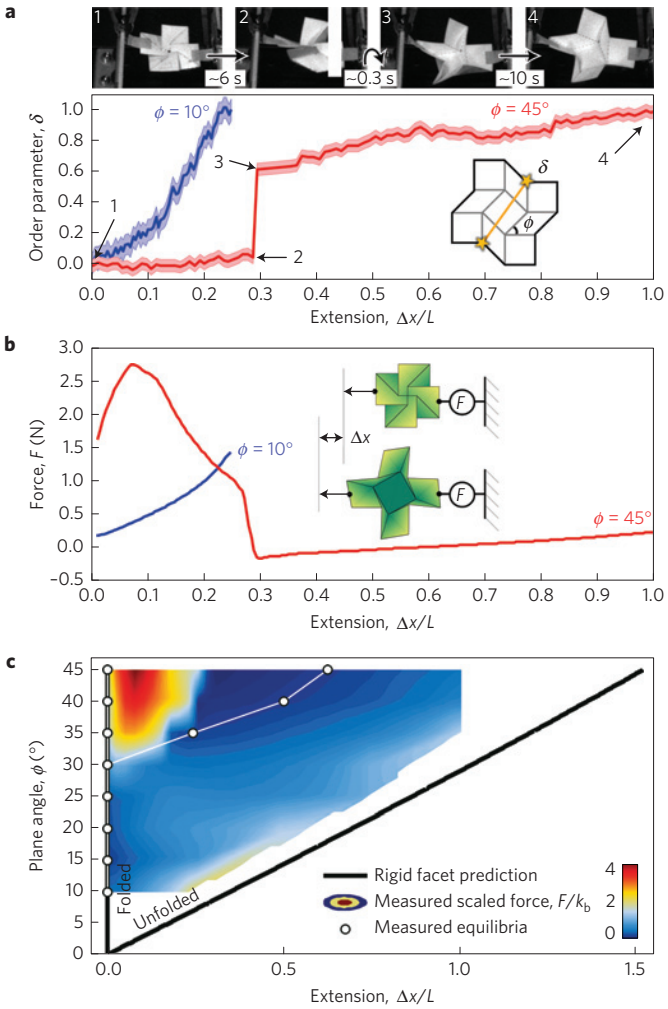

Figure 2 | Experimental strain-controlled mechanical data studying the transition between mono- and bistability in square twists. **a**, Measurements of the folding order parameter, δ, show smooth continuous behaviour for $\phi = 10°$ and an abrupt discontinuous jump for $\phi = 45°$. The inset illustrates the definition of δ, and photographs show points of interest on the red curve. **b**, Measurements of the tensile force F as a function of the normalized extension, $\Delta x/L$, reveal mechanical bistability between folded and unfolded configurations for $\phi = 45°$ and monostability for $\phi = 10°$. The inset shows schematics of the experiment, definition of Δx, and location of the load cell. **c**, Measurements of the tensile force, $F(\phi, \Delta x/L)$, normalized by the sheet's torsional bending stiffness, k_b, show the transition between mono- and bistability. White circles indicate mechanically stable values of $\Delta x/L$, and black lines show predicted solutions based on a crease geometry with rigid facets. Note that these predictions do not permit solutions anywhere off the lines. Furthermore, these data closely correspond to the measurements in Fig. 1c, where load-free stable values of x were plotted as red dots, and where the predicted solutions based on a rigid-facet geometry were similarly shown as black lines.

To study the unfolding behaviour, we measured the mechanical response of the folded square twist to uniaxial tension. We observe remarkably different behaviours for ϕ above and below the critical plane angle ϕ_c. Below ϕ_c, the structure smoothly opens and closes, as indicated by the folding order parameter δ (Fig. 2a inset and blue line; Supplementary Movie 1), whereas above ϕ_c a rapid snapping action between folded and unfolded states is observed, as indicated by a jump in δ (Fig. 2a, red line; Supplementary Movie 2). In the latter case, where $\phi > \phi_c$, both folded and unfolded configurations are stable to small external loading, whereas intermediate configurations are unstable and quickly snap to one state or the other. Displacement-controlled measurements of the force F as a function of ϕ and normalized extension $\Delta x/L$ also showed qualitatively different behaviour above and below ϕ_c (Fig. 2b and inset). Here, the extension Δx is the change in x at a given force F along the direction of loading (Methods). For structures with $\phi < \phi_c$ the force curves

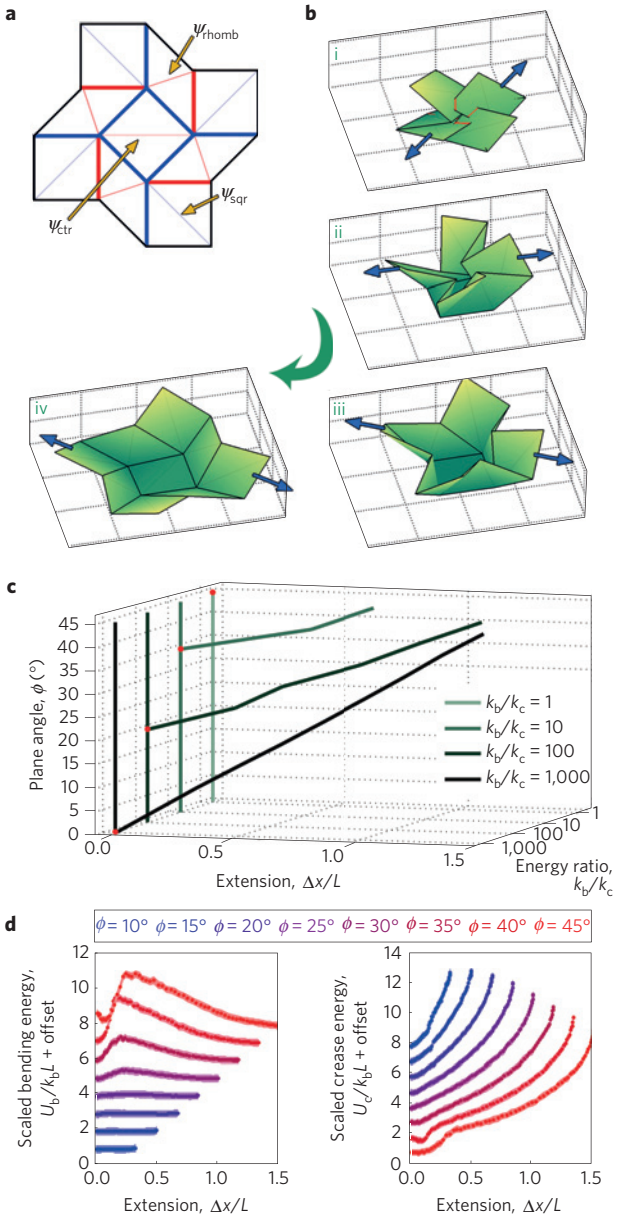

Figure 3 | Simulation results for the square twist with non-rigid facets. **a**, The square-twist crease diagram has been modified with 'virtual creases' that mimic the behaviour of facet bending, as indicated by thin lines. **b**, 3D renderings from the simulation illustrate the unfolding sequence. Blue arrows indicate the external load corresponding to strain-controlled conditions. **c**, Simulation data where each line represents the mechanically stable extensions as a function of geometry for various material properties. The data reveal a critical angle ϕ_c (red dots) that varies with the bending-to-crease energy ratio k_b/k_c. For $k_b/k_c = 1$, monostability is observed for all ϕ, whereas for $k_b/k_c = 10^3$ bistability is found for all ϕ. Between these limits, a bifurcation separating the monostable ($\phi < \phi_c$) and bistable ($\phi > \phi_c$) limits of the phase transition can be found. **d**, Examining the distribution of energy between crease and bending degrees of freedom for $k_b/k_c = 10^2$ as a typical example, we see that the contribution from bending has an energy barrier for intermediate values of $\Delta x/L$ that increases in magnitude with ϕ. Conversely, the energetic contribution from crease opening essentially increases monotonically with $\Delta x/L$ for all ϕ. In both energy plots, the band thickness indicates the simulation uncertainty.

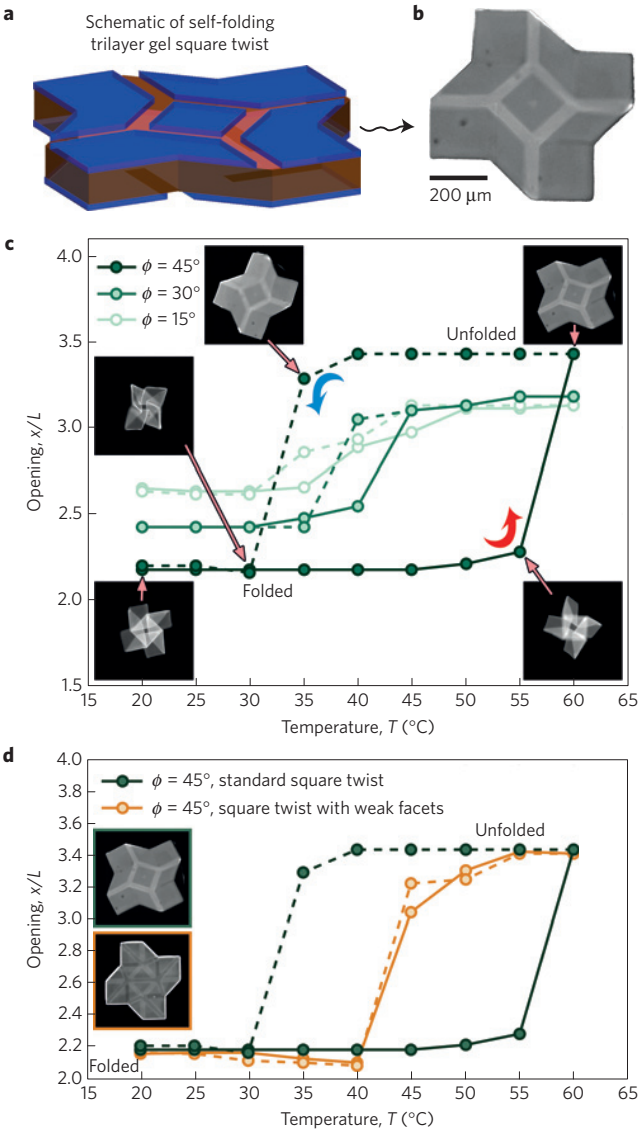

Figure 4 | A sub-millimetre-scale self-folding polymer-gel version of the square twist is used to verify the geometric nature of bistability in stress-controlled conditions. **a**, Schematic of the trilayer structure (dimensions not to scale). Folding is actuated by a temperature-dependent swelling of the middle (pink) layer. Open slits patterned in the top and bottom layers (blue) induce mountain and valley creases, respectively, when viewed from above. **b**, Optical micrograph of a square twist released in an aqueous medium at 60 °C. **c**, Measurements of square-twist opening as a function of temperature demonstrate hysteretic folding/unfolding behaviour for $\phi > \phi_c$ and non-hysteretic folding/unfolding for $\phi < \phi_c$. In this case, $15° < \phi_c < 30°$. Solid lines (unfolding) correspond to heating, and dashed lines (folding) to cooling. Inset micrographs show a structure with $\phi = 45°$ at the indicated measurement points. **d**, Measurements of opening as a function of temperature for the standard square twist compared to a version with creases added where bending would otherwise occur. The additional DOF afforded by setting $k_b/k_c \lesssim 1$ entirely remove hysteretic folding behaviour.

increase monotonically, whereas structures with $\phi > \phi_c$ exhibit force curves with regions of negative slope, indicating mechanical instability. To determine the force landscape that drives transitions from the folded to the unfolded state, we measured the tensile force normalized by the sheet's torsional bending stiffness, k_b (Fig. 2c, Supplementary Figs 3 and 4). We find that the force barrier between these states increases in magnitude with ϕ, hinting at an underlying mechanism for bistability. In particular, facet bending is localized to the rhombi short diagonals, forming 'virtual creases' with a deflec-

tion angle ψ and energy $\sim Lk_b \sin(\phi/2)\psi^2$. Because the length of these diagonals increases with ϕ, the force barrier increases as well.

To further investigate this facet-bending mechanism, we developed a numerical simulation of the unfolding behaviour under uniaxial tension that calculates the configuration minimizing the facet-bending and crease-unfolding energies for a given ϕ and $\Delta x/L$ (Fig. 3a,b, Methods). From these calculations, we determine the energetic minima, which correspond to mechanically stable states, for different ratios of the bending and crease torsional spring constants, k_b/k_c (Fig. 3c). For $k_b/k_c \leq 1$, monostability was observed for all geometries, whereas for $k_b/k_c \geq 10^3$, all geometries exhibited bistability. Between these limits, we found a critical plane angle ϕ_c marking a bifurcation between mono- and bistability that varied with k_b/k_c. When compared with the experimental phase diagram (Fig. 2c), these calculations predict $10 < k_b/k_c < 100$, which is consistent with measurements that found $k_b/k_c \simeq 36$ for the paper used in experiments (Supplementary Information).

Examining the internal distribution of energy by separating the dimensionless bending energy U_b/k_bL from the dimensionless crease energy U_c/k_bL sheds light on how different DOF are interacting to tune the bifurcation (Fig. 3d). For example, taking $k_b/k_c = 10^2$, where $\phi_c \approx 20°$, we see that the system's total bending energy has an energy barrier at intermediate values of $\Delta x/L$ whose magnitude increases with ϕ. The total crease energy, on the other hand, monotonically increases with $\Delta x/L$ for all ϕ. Whether this monotonic rise in crease energy is high enough to overcome the energy barrier that arises from hidden bending DOF determines if the system is mono- or bistable (Supplementary Fig. 5).

Collectively, these results provide a geometric understanding for the mechanical bistability of the square twist and, as such, should translate to any thin sheet folded according to this crease pattern. Although our experiments were performed with strain-controlled loading, we predict that the observed bifurcation will give rise to a hysteretic behaviour under stress-controlled loading that can be tuned by both ϕ and k_b/k_c. To test this prediction, we used a micropatterned gel-trilayer version of the square twist with $L = 200\,\mu m$ (Fig. 4a,b; Methods). Here, differential swelling between gel layers is used to create internal stresses that fold and unfold the structure as the temperature T is varied. For this system, we estimate $k_b/k_c \sim 10^2$ (Supplementary Information), and therefore from simulations we expect $\phi_c \approx 20°$ (Fig. 3c). Imaging a square twist with $\phi = 45°$ as the temperature is quasi-statically varied reveals the expected hysteresis (Fig. 4c, dark green line). As predicted, when ϕ is decreased to 30° the hysteresis is reduced (medium green line), and ultimately vanishes for $\phi = 15°$ (light green line). Our results with paper models and simulations also suggest that hysteretic folding behaviour can be removed if $k_b/k_c \lesssim 1$. This scenario can be realized in the gel sheets by modifying and fully triangulating the crease pattern (for example, Fig. 3a), effectively placing creases where bending would otherwise occur. Indeed, we find for $\phi = 45°$ that the addition of these creases removes the hysteresis (Fig. 4d). These experiments clearly illustrate the first-order properties of the transition between folded and unfolded states that arises from hidden bending DOF in the square twist (Supplementary Fig. 6).

Although this work shows how hidden DOF can be used to create non-trivial features in an origami structure's configuration space, we envisage that the tunable and scale-free nature of the square twist's bistability should make it a useful design for robotic grippers, microfluidic devices and even wearable exoskeletons. Moreover, because the square twist can form 2D tessellations, it should be possible to spatially vary the unit-cell geometry to create origami mechanical metamaterials. For example, in analogy with secondary structures in polymers that provide hidden length[31], the ability of the pattern to resist deformation up to a predetermined force threshold can be taken advantage of to make materials with extremely high toughness. Such devices would be capable of large bulk strain without fracture by absorbing energy in a predetermined pattern of sequentially opening square-twist unit cells. More broadly, the possibility of alternative geometries (Supplementary Fig. 7) and additional hidden DOF—such as facet stretching, facet shearing and crease torquing—suggests that an even richer configuration space may be hidden with these more energetically expensive deformation modes. For example, these ideas are found in the mechanics of thin shells, where bending and stretching energy barriers have been shown to be modified by the introduction of creases[32], leading to a broad range of multistable behaviours. Thus, the geometry of creased sheets offers a simple experimental platform to probe the mechanical behaviour of a wider class of constraint-based materials and the consequences of energy-scale dependent DOF.

Methods

Sample fabrication and characterization. Digital CAD software and a laser cutter were used to fabricate square-twist structures from 120 lb paper (Radiance 120 lb super smooth card stock, Beckett Expressions). Creases were patterned by cutting perforated lines with equal lengths of material and gaps, then folded by hand with a Lineco bone scorer to be mountain or valley according to the crease assignment (Fig. 1a). For these samples, we set $L = 2.54$ cm and varied ϕ from 10° to 45° in increments of 5°. The lower bound is the limit of what can be reasonably folded from this material, although a theoretical limit of 0° is where the crease pattern is no longer well defined owing to overlapping mountain and valley curves. The upper bound is set by self-intersection, which prevents the structure from folding flat for $\phi > 45°$. Samples used throughout this work were folded and unfolded before mechanical testing, thus the unfolded stable configuration retains some folding along the creases owing to plastic deformation and hence responds differently than a 'pristine' sheet that has never been folded.

To quantify a square twist's configuration in the absence of load, each sample was first folded flat, then held to a calliper ruler to measure the Euclidean distance x (Fig. 1a). Subsequently, each sample was unfolded, flattened on a table under 2 s of compression applied by hand, and the distance x remeasured.

A custom-built mechanical tester previously described[5] was used to measure the mechanical properties of square twists under tension. Samples were fixed to the testing device and suspended in air with small tabs of gaffing tape. Although this pre-loaded the samples with minor tension at zero extension (Fig. 2a), this approach prevented any interactions with the lower surface of the testing apparatus, which would otherwise interfere with the unfolding process. In a typical experiment, the distance between loading plates and load cell force data were simultaneously recorded by a single custom MATLAB program, and the data stored for later analysis. Furthermore, the maximum experimental extension was kept smaller than the theoretical limits (Fig. 2c black lines) to reduce risk of tearing samples apart. Sample testing was video recorded with a Canon Powershot camera filming at 7.5 FPS. Standard image analysis techniques were used to measure the order parameter for folding, δ, as a function of the normalized extension $\Delta x/L$, which as described in the main text is measured from the mechanically equilibrated folded state (Fig. 1c lower branch of red data).

Simulated square twists. To explore how material properties, and in particular finite bending stiffness of the flat facets, influences mechanical behaviour of the system, we developed a numerical simulation of the square twist's folding behaviour. In it, we constrained each of the 16 facet corners to have a fixed distance from their neighbouring corners according to the crease pattern. Crease and facet bending deformations were then assigned an elastic energy given by:

$$\begin{aligned} U_{total} &= U_{crease} + U_{bend} \\ &= \frac{L}{2}\left[k_c \sum_{i=1}^{12}(\theta_i - \theta_0)^2 + k_b \sum_{j=1}^{9} \lambda_j \psi_j^2\right] \end{aligned} \quad (1)$$

where

$$\lambda_j = \begin{cases} \sqrt{2} & \text{for square facets,} \\ 2\sin(\phi/2) & \text{for rhombus facets} \end{cases}$$

In this expression, the first term is the crease energy, which is proportional to the torsional elastic constant k_c times the crease length L, and is a sum over the 12 individual creases. It is also a function of the crease angle θ, determined from a dot product of two adjacent facet normals, minus an equilibrium value θ_0. This represents the fact that, once made, creases no longer lay flat. A value of $\theta_0 = 10°$ was used here, which is consistent with our experimental samples. The second term is the facet-bending energy, which is proportional to the torsional elastic constant k_b times the length of the bend $\lambda_j L$, and is a sum over the nine indicated facet diagonals (Fig. 3a). It is a function of the bending angle ψ_j, which, unlike creases, is zero in a stress free state. Like the crease DOF, these bending DOF are also calculated from the dot product of the facet normals.

Specifying ϕ and a target $\Delta x/L$, equation (1) was numerically minimized using the Levenberg–Marquardt algorithm in MATLAB, where the target $\Delta x/L$ was incremented from 0 to its maximum value in 91 steps. This process was repeated 20 times with initial conditions generated from a geometric interpolation between the folded and unfolded states that did not preserve facet areas. In each realization, the facet corners were perturbed along x, y and z by an amount that was uniformly distributed over the range given by $\pm L/10$. In this way, we used semi-random initial conditions to form an ensemble-averaged solution that minimized equation (1) and satisfied the crease pattern's geometric constraints. We then averaged the facet bending angles of the ensemble-averaged solution, producing an overall average rhombus bending angle ψ_{rhomb}, an overall average square-facet bending angle ψ_{sqr}, and a centre square-facet bending angle ψ_{ctr} (Supplementary Information).

Self-folding gel fabrication and imaging. The self-folding version of the square twist consists of a temperature-responsive hydrogel film capped on both the top and bottom surfaces by rigid patterned layers. Although the method is described elsewhere[33], we provide a brief summary here. First, we spin-coated a layer of ultraviolet-crosslinkable poly(*p*-methyl styrene) (PpMS) with a thickness of 50 nm. Using a maskless lithographic method, a pattern of stripes corresponding to the valley creases was used to define regions where the PpMS layer was crosslinked. Next, the temperature-responsive poly(*N*-isopropyl acrylamide-*co*-sodium acrylate) (PNIPAM) polymer was deposited and crosslinked on the PpMS layer with a thickness of 1.5 µm. Finally, a second layer of PpMS with a thickness of 50 nm was deposited and crosslinked with a pattern corresponding to the mountain creases. This trilayer structure then consisted of two thin rigid outer layers encompassing a middle layer that swells with temperature. To prevent adhesion between the hydrophobic PpMS panels in the folded state, a 10-nm polyelectrolyte layer was coated on both outer surfaces of PpMS by spin-coating a photo-crosslinkable poly(sulphopropyl methacrylate) copolymer and crosslinking with ultraviolet light. On swelling in an aqueous buffer, stresses are developed within the middle hydrogel layer, causing the bilayer crease-like regions to bend to an angle programmed by the width of the open stripe in the capping PpMS layer. Trilayer regions, on the other hand, remain flat like facets. For the square-twist pattern, each crease segments is programmed to fold to either $\pm\pi$ at room temperature, corresponding to the flat folded state.

Full triangulation of the fold pattern was accomplished by patterning open stripes in both the top and bottom rigid films where bending was observed in the paper experiments and numerical simulations. Thus, these regions had only a single layer gel film that was not programmed to fold, but instead offered much lower bending resistance than the trilayer facet regions.

To measure the opening x, each sample was placed in an aqueous medium and observed with epi-fluorescence microscopy through the temperature range 20 to 60 °C. A heat stage was used to control the temperature (Zeiss Tempcontrol 37-2 digital), which was varied in 5 °C increments. At least 30 min at each temperature was allowed for the gel to swell to equilibrium. The folding/unfolding process, therefore, was under quasi-static stress-controlled conditions. 3D images of polymer square twist were reconstructed using ImageJ from image stacks collected using a laser scanning confocal fluorescence microscope (Zeiss LSM 510 META), with the refractive index of the aqueous medium corrected for.

Received 28 November 2014; accepted 30 January 2015; published online 9 March 2015

References

1. Greenberg, H., Gong, M., Magleby, S. & Howell, L. Identifying links between origami and compliant mechanisms. *Mech. Sci.* **2,** 217–225 (2011).
2. Song, J., Chen, Y. & Lu, G. Axial crushing of thin-walled structures with origami patterns. *Thin. Walled Struct.* **54,** 65–71 (2012).
3. Schenk, M. & Guest, S. D. Geometry of miura-folded metamaterials. *Proc. Natl Acad. Sci. USA* **110,** 3276–3281 (2013).
4. Wei, Z. Y., Guo, Z. V., Dudte, L., Liang, H. Y. & Mahadevan, L. Geometric mechanics of periodic pleated origami. *Phys. Rev. Lett.* **110,** 215501 (2013).
5. Silverberg, J. L. *et al.* Using origami design principles to fold reprogrammable mechanical metamaterials. *Science* **345,** 647–650 (2014).
6. Waitukaitis, S., Menaut, R., Chen, B. G-g. & van Hecke, M. Origami multistability: From single vertices to metasheets. *Phys. Rev. Lett.* **114,** 055503 (2015).
7. Lv, C., Krishnaraju, D., Konjevod, G., Yu, H. & Jiang, H. Origami based mechanical metamaterials. *Sci. Rep.* **4,** 5979–5981 (2014).
8. Hanna, B. H., Lund, J. M., Lang, R. J., Magleby, S. P. & Howell, L. L. Waterbomb base: A symmetric single-vertex bistable origami mechanism. *Smart Mater. Struct.* **23,** 094009 (2014).
9. Huffman, D. A. Curvature and creases: A primer on paper. *IEEE Trans. Comput.* **25,** 1010–1019 (1976).
10. Tachi, T. in *Proceedings of the International Association for Shell and Spatial Structures (IASS) Symposium: Evolution and Trends in Design, Analysis and Construction of Shell and Spatial Structures* (eds Domingo, A. & Lazaro, C.) 2287–2294 (Editorial Universitat Politècnica de València, 2009); http://go.nature.com/HbzSH1
11. Hull, T. *Project Origami: Activities for Exploring Mathematics* (CRC Press, 2012).
12. Thiria, B. & Adda-Bedia, M. Relaxation mechanisms in the unfolding of thin sheets. *Phys. Rev. Lett.* **107,** 025506 (2011).
13. Dias, M. A., Dudte, L. H., Mahadevan, L. & Santangelo, C. D. Geometric mechanics of curved crease origami. *Phys. Rev. Lett.* **109,** 114301 (2012).
14. Lechenault, F., Thiria, B. & Adda-Bedia, M. Mechanical response of a creased sheet. *Phys. Rev. Lett.* **112,** 244301 (2014).
15. Feng, S. & Sen, P. N. Percolation on elastic networks: New exponent and threshold. *Phys. Rev. Lett.* **52,** 216–219 (1984).
16. Broedersz, C. P., Mao, X., Lubensky, T. C. & MacKintosh, F. C. Criticality and isostaticity in fibre networks. *Nature Phys.* **7,** 983–988 (2011).
17. Silverberg, J. L. *et al.* Structure-function relations and rigidity percolation in the shear properties of articular cartilage. *Biophys. J.* **107,** 1–10 (2014).
18. Sun, K., Souslov, A., Mao, X. & Lubensky, T. Surface phonons, elastic response, and conformal invariance in twisted kagome lattices. *Proc. Natl Acad. Sci. USA* **109,** 12369–12374 (2012).
19. Kane, C. & Lubensky, T. Topological boundary modes in isostatic lattices. *Nature Phys.* **10,** 39–45 (2013).
20. Chen, B. G-g., Upadhyaya, N. & Vitelli, V. Nonlinear conduction via solitons in a topological mechanical insulator. *Proc. Natl Acad. Sci. USA* **111,** 13004–13009 (2014).
21. Paulose, J., Chen, B. G-g. & Vitelli, V. Topological modes bound to dislocations in mechanical metamaterials. *Nature Phys.* **11,** 153–156 (2015).
22. Liu, A. J. & Nagel, S. R. Nonlinear dynamics: Jamming is not just cool any more. *Nature* **396,** 21–22 (1998).
23. Keys, A. S., Abate, A. R., Glotzer, S. C. & Durian, D. J. Measurement of growing dynamical length scales and prediction of the jamming transition in a granular material. *Nature Phys.* **3,** 260–264 (2007).
24. Van den Wildenberg, S., van Loo, R. & van Hecke, M. Shock waves in weakly compressed granular media. *Phys. Rev. Lett.* **111,** 218003 (2013).
25. Thorpe, M. Continuous deformations in random networks. *J. Non-Cryst. Solids* **57,** 355–370 (1983).
26. Heyman, J. *The Science of Structural Engineering* (World Scientific, 1999).
27. Maxwell, J. C. On the calculation of the equilibrium and stiffness of frames. *Lond. Edinb. Dubl. Phil. Mag. J. Sci.* **27,** 294–299 (1864).
28. Calladine, C. Buckminster Fuller's "tensegrity" structures and Clerk Maxwell's rules for the construction of stiff frames. *Int. J. Solids Struct.* **14,** 161–172 (1978).
29. Demaine, E. D., Demaine, M. L., Hart, V., Price, G. N. & Tachi, T. (Non) existence of pleated folds: How paper folds between creases. *Graphs Combinator.* **27,** 377–397 (2011).
30. Hull, T. C. *Origami*^{3}*: Proceedings of the Third International Meeting of Origami Science, Mathematics, and Education* 29–38 (A K Peters, 2002).
31. Fantner, G. E. *et al.* Sacrificial bonds and hidden length: Unraveling molecular mesostructures in tough materials. *Biophys. J.* **90,** 1411–1418 (2006).
32. Bende, N. P. *et al.* Geometrically controlled snapping transitions in shells with curved creases. Preprint at http://arxiv.org/abs/1410.7038 (2014).
33. Na, J-H. *et al.* Programming reversibly self-folding origami with micropatterned photo-crosslinkable polymer trilayers. *Adv. Mater.* **27,** 79–85 (2015).

Acknowledgements

The authors thank J. Mosely, U. Nguyen, B. Johnson, B. Parker and M. Schneider for artistic inspiration, as well as O. Vincent, N. Bende, C-K. Tung, S. Waitukaitis and the Cohen lab for useful discussions. We also thank F. Parish for assistance with the laser cutter. This work was funded by the National Science Foundation through award EFRI ODISSEI-1240441.

Author contributions

J.L.S., J-H.N., R.C.H. and I.C. designed the research; J.L.S., J-H.N. and A.A.E. conducted the research and interpreted the results; B.L., T.C.H., C.D.S., R.J.L., R.C.H. and I.C. supervised the research and interpreted the results; J.L.S., J-H.N., A.A.E., T.C.H., R.J.L. and I.C. prepared the manuscript.

Additional information

Supplementary information is available in the online version of the paper. Reprints and permissions information is available online at www.nature.com/reprints. Correspondence and requests for materials should be addressed to J.L.S.

Competing financial interests

The authors declare no competing financial interests.

nature materials

SUPPLEMENTARY INFORMATION

DOI: 10.1038/NMAT4232

Origami structures with a critical transition to bistability arising from hidden degrees of freedom

Jesse L. Silverberg,[1,*] Jun-Hee Na,[2] Arthur A. Evans,[3] Bin Liu,[1] Thomas C. Hull,[4] Christian D. Santangelo,[3] Robert J. Lang,[5] Ryan C. Hayward,[2] and Itai Cohen[1]

[1] *Physics Department, Cornell University, Ithaca, NY 14853, USA*
[2] *Department of Polymer Science and Engineering, University of Massachusetts, Amherst, MA 01003, USA*
[3] *Department of Physics, University of Massachusetts, Amherst, MA 01003, USA*
[4] *Department of Mathematics, Western New England University, Springfield, MA 01119, USA*
[5] *Lang Origami, Alamo, CA 94507*

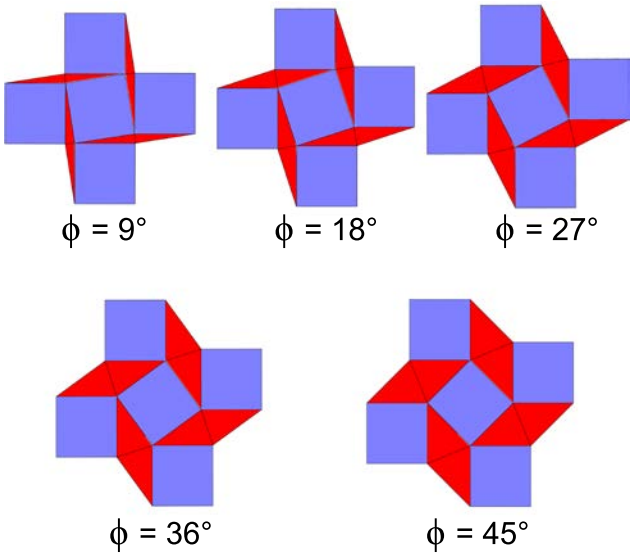

FIG. S1. These schematics show crease patterns for square twists with various plane angles.

ADDITIONAL SCHEMATICS

To supplement the crease pattern shown in the main text where the plane angle $\phi = 45°$, additional fold patterns are shown here with different plane angles ϕ (Fig. S1).

COUNTING SQUARE TWIST DOF

The number of DOF for a generic polyhedral surface in 3D with no holes can be derived from Euler's polyhedral formula and is expressed as[1,2]

$$\mathrm{DOF} = N_{E,b} - 3 - \sum_{N_{f,i}>3} (N_{f,i} - 3), \qquad \text{(S1)}$$

where $N_{E,b}$ is the number of edges on the boundary and $N_{f,i}$ is the number of edges of the i^{th} facet. For the generic square twist (Fig. 1(a) and S1), $N_{E,b} = 12$, $N_{f,i} = 4$ for $i = 1, \ldots, 9$, giving zero DOF. This is consistent with the observation that the *generic* quad mesh is locked, and thus has no flexibility. As is well-known, there are special non-generic quad meshes such as the Miura-ori[3] for which symmetry makes some constraints redundant. For the Miura-ori this restores one DOF, but in general, more DOF can be restored depending on the specific symmetries. Along these lines, square twists with modified mountain and valley crease assignments are known to be rigidly foldable with one DOF[4].

PREDICTED SOLUTIONS FOR RIGID FACETS

Given the crease pattern alone, a trigonometric analysis reveals the square twist should have two configurations corresponding to the folded and unfolded states. Defining the angle Θ to be any of the valley creases on the interior square facet, we calculate the distance between the two points that define the folding order parameter δ and find the constraint $\cos^2\Theta = 1$. Thus, $\Theta = 0$ or π, which respectively, is the unfolded and folded configurations. Taking a similar approach and calculating $\Delta x/L$, we find

$$\Delta x/L = \Big[\big(1 + 2\cos\phi \pm \sin\phi\big)^2 + \big(\pm 1 + 2\sin\phi \mp \cos\phi\big)^2\Big]^{1/2}, \qquad \text{(S2)}$$

which was used to plot the two black contours in Fig. 1(c) of the main text.

MODIFIED SQUARE TWIST WITH 1 DOF

As a simple way to explore the role of bending DOF in the square twist independent of the role played by energetics, we extend the rigid facet geometric model to permit bending along the short diagonals of each rhombus, effectively splitting them into two rigid isosceles triangles. Imposing 4-fold rotational symmetry constrains the crease pattern so that only 1 DOF is added to the system. Using MATLAB, we sweep through ϕ from 0° to 45° in steps of 2.5° and solve for the folding order parameter δ as the rhombus facet bending angle ψ_{rhomb} is varied. We take a maximum deflection of ψ_{rhomb} to

DOI: 10.1038/NMAT4232

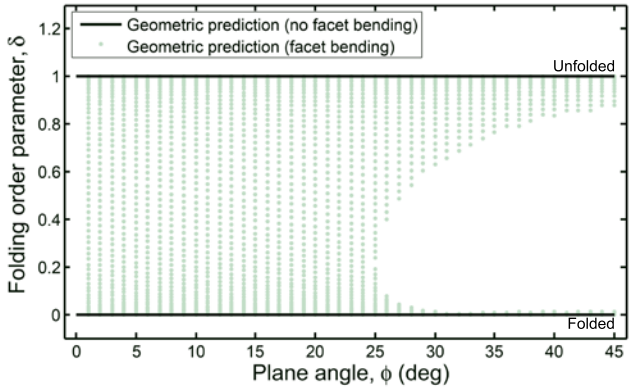

FIG. S2. Bifurcation of the folding order parameter δ when 1 DOF is added from facet bending. For a rigid square twist, $\delta = 0$ when folded, 1 when unfolded, and due to geometric constraints forbidden from taking any intermediate value (black lines). Introducing bending allows δ to take intermediate values (green dots) with a critical point at $\phi_c = (23 \pm 2)^\circ$ that separates a continuously connected region ($\phi < \phi_c$) from a region with disconnected solutions ($\phi > \phi_c$). Green points are uniformly spaced in the bending angle ψ_{rhomb}, and the forbidden configurations ($\phi > \phi_c$, white space) corresponds to the region with rapid unfolding dynamics (Fig. 2(a), main text).

be 10° and plot the solutions in the (δ, ϕ) configuration space (Fig. S2). In contrast to the experiments and detailed mechanical simulation described in the main text, each crease DOF here has a bending stiffness $k_c = 0$, and each bending DOF has $k_b = 0$ for $\psi_{\text{rhomb}} \leq 10^\circ$ and $k_b = \infty$ for $\psi_{\text{rhomb}} > 10^\circ$. Though this constrained bending DOF is a coarse model for how bending works in real materials, it allows us to isolate kinetic properties of the structure and their consequences for configuration space. Indeed, similar to experimental observations, we find a bifurcation at $\phi_c = (23 \pm 2)^\circ$ with monostability for $\phi < \phi_c$, and bistability for $\phi > \phi_c$. Evidently, the extra DOF introduced by facet bending is a major factor that enables both the ϕ-dependent bifurcation and foldability of the square twist.

MEASURING FLEXURAL RIGIDITY

To normalize experimental force and energy data, the flexural rigidity D was measured from a strip of 120 lb paper whose dimensions were $L \times 8.5L$, with $L = 2.54$ cm. To make this measurement, the strip was clamped horizontally, allowing a controlled length to be suspended under gravity. Digital photographs were taken from a side view so that the strip could be seen edge-on and its deflection determined (Fig. S3(a)). Thus, we captured a series of images where the suspended arc length ℓ varied from L to $8L$, and with standard image tracking techniques, we extracted the vertical deflection y as a function of horizontal position x (Fig. S3(b), red line). This coordinate data was fit to the expression[5]

$$y = \left(\frac{\rho g t}{24 D}\right)\left(x^4 - 4\ell x^3 + 6\ell^2 x^2\right), \qquad \text{(S3)}$$

where ρ is the measured paper density and t is the measured paper thickness (Fig. S3(c,d)). Eq. (S3) was derived for the small deflection limit and allowed us to perform a one-parameter fit for D as ℓ was varied from L to $8L$. Generally, measurements for $\ell < 2L$ were dominated by an intrinsic curvature in the paper. For $\ell = 8L$ there were also noticeable deviations from to the small-deflection approximation used to derive Eq. (S3). For all other values of ℓ, the fits were tightly clustered around the median measured D. Flipping the strip over and repeating the measurements on the opposite side produced another set of values for D as a function of ℓ that exhibited the same trends. Averaging the median values from each data set yielded the value used in the main text, $D = (15.6 \pm 0.7) \times 10^{-3}$ N·m, where $t = 0.356$ mm and $\rho = 871$ kg/m^3.

To convert the flexural rigidity D to the bending torsional elastic constant k_b, we note that bending is constrained by the crease pattern to occur over an area of length L and width s. Here, s is the bending arc length and, to a good approximation, is $s \simeq L/10$ for our experiments. Thus, the bending energy is $U_b = (D/2)\int R^{-2}\, dA$, where the radius of curvature $R = s/\psi$ and the integral is evaluated over the area where bending occurs. Approximating R as constant over the bend, we evaluate the integral and find $U_b = (DL/2s)\psi^2 \equiv (L/2)k_b\psi^2$. Thus, $k_b = D/s \simeq 6$ N/rad.

SQUARE TWISTS WITH DIFFERENT THICKNESS PAPER

In the main text data was presented on 120 lb paper (Fig. 2(b)). Here, we provide measurements of the tensile force F as a function of plane angle ϕ and normalized extension $\Delta x/L$ for 53 lb ($D = 2.1 \times 10^{-3}$ N·m) and 28 lb ($D = 0.53 \times 10^{-3}$ N·m) paper (Fig S4).

MEASURING CREASE TORSIONAL STIFFNESS

A single mountain crease 21.6 cm in length was made in a sheet of 120 lb paper and loaded into our custom mechanical testing device[3]. The crease was deflected by 0.94 rad and found to have two linear responses corresponding to small (< 0.15 rad) and large (> 0.15 rad) deflections. For the small deflections characteristic of an elastic response, the torque was linearly proportional to angular deflection by a constant $k_c = 170 \pm 20$ mN/rad, which we take as the crease torsional stiffness.

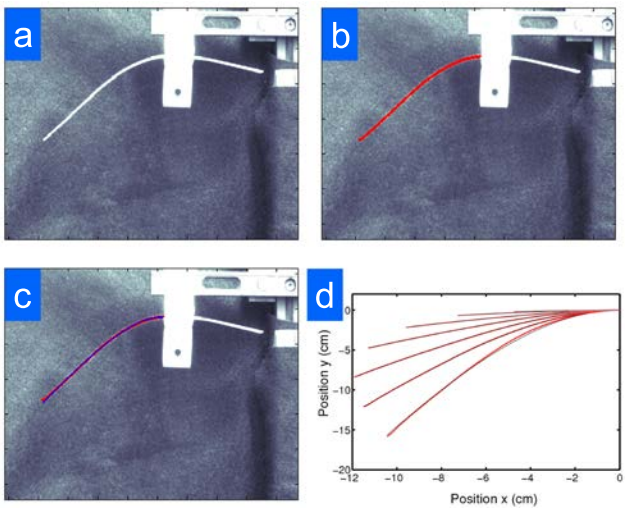

FIG. S3. Steps for measuring the flexural rigidity, D. (a) A strip of paper is clamped horizontally and allowed to sag under gravity. A photograph of the deflection is taken from the edge view, which extends to the left of the mounting armature. (b) Standard image analysis techniques are used to extract the vertical deflection, y, as a function of the horizontal position, x. The red line is the automatically tracked coordinate data superimposed on the corresponding photograph. (c) The measured deflection $y(x)$ is fit to Eq. (S3) and is shown here in blue for comparison. (d) The process of fitting the deflection to Eq. (S3) is repeated for various lengths L of paper. This plot superimposes measured deflection for one strip of 7 lengths (red) and best-fits (black). As the fits are nearly indistinguishable from the data, we find this is a highly reliable method to determine D.

SIMULATION AND EXPERIMENTAL ENERGY PLOTS

In the main text, we examined the bifurcation between mono- and bistability in terms of mechanically stable equilibrium points. Here, we provide an alternative and equivalent comparison presented in terms of the energy as a function of plane angle ϕ and extension $\Delta x/L$ (Fig. S5). Specifically, the normalized total energy in simulation and experiments both have a single local energy minimum below the critical plane angle and two energy minima above the critical plane angle. These minima correspond to the mechanically stable equilibrium points described in the main text.

ESTIMATION OF SELF-FOLDING GEL k_b AND k_c

For the self-folding gel sheets, considerations from continuum elasticity show the creases have an energy scale[6]

$$U_{\text{gel crease}} \sim \bar{E}_{\text{gel}} t_{\text{gel}}^3, \tag{S4}$$

while the facets have a bending energy scale

$$U_{\text{gel facet}} \sim \bar{E}_{\text{rigid}} t_{\text{rigid}} t_{\text{gel}}^2. \tag{S5}$$

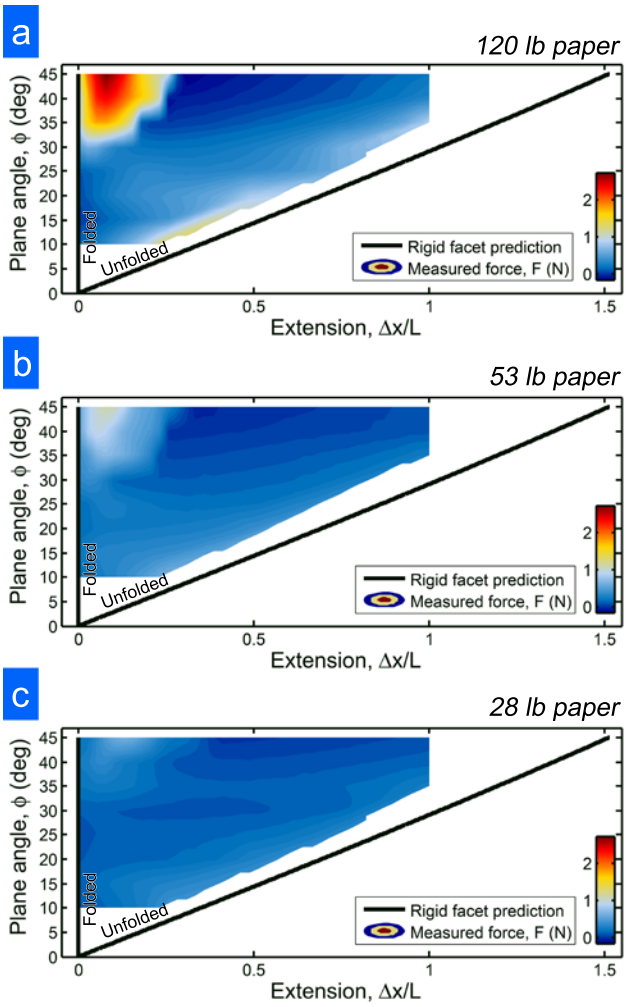

FIG. S4. Experimental strain-controlled mechanical data studying the transition between mono- and bistability in square twists. Measurements of the tensile force $F(\phi, \Delta x/L)$ for (a) 120 lb paper, (b) 53 lb paper, and (c) 28 lb paper show the transition between mono- and bistability is generic, though the force barrier for $\phi > \phi_c$ dramatically decreases as the paper becomes thinner.

Taking the PNIPAM gel plane-strain modulus $\bar{E}_{\text{gel}} \sim 10^6$ Pa, the gel's thickness $t_{\text{gel}} \sim 10^{-6}$ m, the plane-strain modulus of the rigid PpMS layer $E_{\text{rigid}} \sim 10^9$ Pa, and the PpMS layer thickness $t_{\text{rigid}} \sim 10^{-7}$ m, we find

$$\frac{U_{\text{gel facet}}}{U_{\text{gel crease}}} \sim \frac{k_b}{k_c} \sim 10^2, \tag{S6}$$

as was used in the main text.

GLOBAL ENERGY MINIMA FOR STRESS-CONTROLLED LOADING

The custom simulation developed in MATLAB and described in the main text was designed to follow the kine-

DOI: 10.1038/NMAT4232

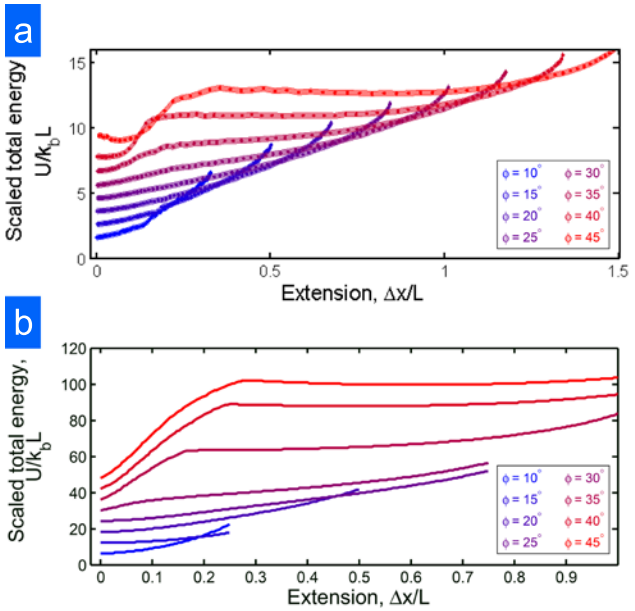

FIG. S5. Dimensionless square twist energy with local minima corresponding to mechanical equilibrium. (a) The sum of crease and bending energy from Fig. 3(d) of the main text shows how the competition between these different deformations gives rise to mono- and bistable regimes. (b) Integrating the experimentally measured force data produces a family of energy curves shown here with an offset, which agrees favorable with simulations.

matics of the square twist along a strain-controlled path in phase space. To determine the stress-controlled equivalent and obtain an independent check of our results, we utilized Tessellatica, a freely available Mathematica package. To implement the folding of the square twist in Tessellatica, we define the crease pattern by defining coordinates for 2D vertices, and assign edges to pairs of vertices with an associated mountain, valley, universal, or boundary attribute (Fig. 6(a)).

Valid folding configurations must obey the Kawasaki consistency conditions, which we briefly describe here. We start by drawing a closed curve around any given vertex and define the matrix A_i that rotates by the sector angle α_i so that the i^{th} crease lies along one of the principal axes. Define the matrix C_i that rotates about the crease by an angle $\pi - \gamma_i$. The entire folded form can then be generated by applying the matrix $\chi_i = A_i C_i A_i^{-1}$ to the i^{th} sector; this matrix rotates the whole sector to the crease, rotates the sector by the fold angle, and then rotates back. The Kawasaki consistency condition states that on a degree N vertex, the rigidity matrix R must satisfy the following[7,8]:

$$R = \chi_1 \chi_2 \cdots \chi_{N-1} \chi_N = \mathcal{I}, \qquad \text{(S7)}$$

where $\mathcal{I}$ is the identity matrix. This gives a system of equations for the the fold angles of a vertex satisfying consistency.

To model the self-folding gel experiments, we start with a flat square twist where every crease angle is 0° at equilibrium, and define the 2D graph accordingly in Tessellatica (Fig. 6(a)). We then set a reference angle for each assigned crease, i.e. Θ_0 for valley creases and $-\Theta_0$ for mountain creases. Facet bending is implemented by setting the target fold angles to zero for these "creases" in the 2D graph. The energy functional as given in the main manuscript is minimized subject to the Kawasaki vertex consistency constraint. The equilibrium opening distance x/L is determined for the case where $k_b/k_c = 50$ as a function of plane angle ϕ and target reference crease angle Θ (Fig. 6(b)). This data shows the existence of a critical point $\phi_c \approx (27.5 \pm 2.5)°$, below which x/L smoothly varies with Θ, and above which, has a discontinuity. Because Tessellatica analytically solves for globally minimized energy structures, we do not recapitulate the hysteresis curves seen in the experimental measurements of self-folding square twists. The existence of the discontinuity in the global energy minimum, however, is precisely the signature that would be expected in light of this software feature.

THE TRIANGLE TWIST

While the work presented here focuses on the square twist, it is not the only crease pattern that exhibits a geometrically-driven bifurcation between mono- and bistability. For example, the modified triangle twist[9] (Fig. S7) exhibits similar features. In this origami pattern, the plane angle θ (Fig. S7(a)) has a critical point at $\approx 67°$. This can be seen by varying θ and plotting the folding angle a, which is 0° when unfolded and 180° when entirely folded. For $\theta > \theta_c$, a continuum of values for a is possible, whereas $\theta < \theta_c$ has disconnected solutions (Fig. S7(b)).

It's interesting to note that this triangle twist is rigidly foldable while the square twist is not. Thus, the continuum of solutions for folding angle a does not require bending, whereas solutions in the geometrically forbidden region with do. This highlights an important point: The bifurcation in both square and triangle twists is a geometrically-driven phenomenon *independent* of whether bending occurs or not during the folding process. The path through this configuration space, however, depends sensitively on bending and crease DOF as well as the separation of energy scales k_b/k_c.

SUPPLEMENTAL VIDEO CAPTIONS

SI Video 1: Demonstration of weak snapping between folded and unfolded states of a square twist with $\phi \approx \phi_c$.

SI Video 2: Demonstration of pronounced snapping instability between folded and unfolded states of a square

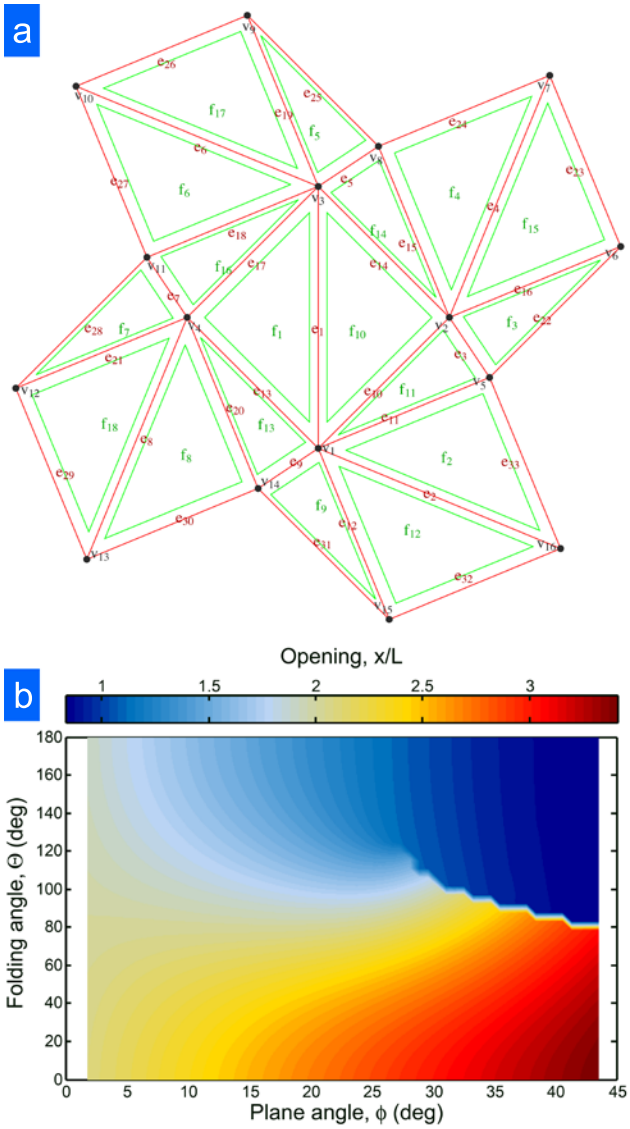

FIG. S6. Input and results from Tessellatica calculations of the stress-controlled square twist. (a) The 2D graph defined in Tessellatica that contains all the information about crease placement and facet bending. (b) Solving for the equilibrium structure as a function of plane angle ϕ, we determine the square twist opening as the equilibrium value of the folding angle Θ is varied from 0° to 180°. This simulates stress-controlled conditions and identifies the presence of a discontinuity at a critical plane angle.

twist with $\phi > \phi_c$.

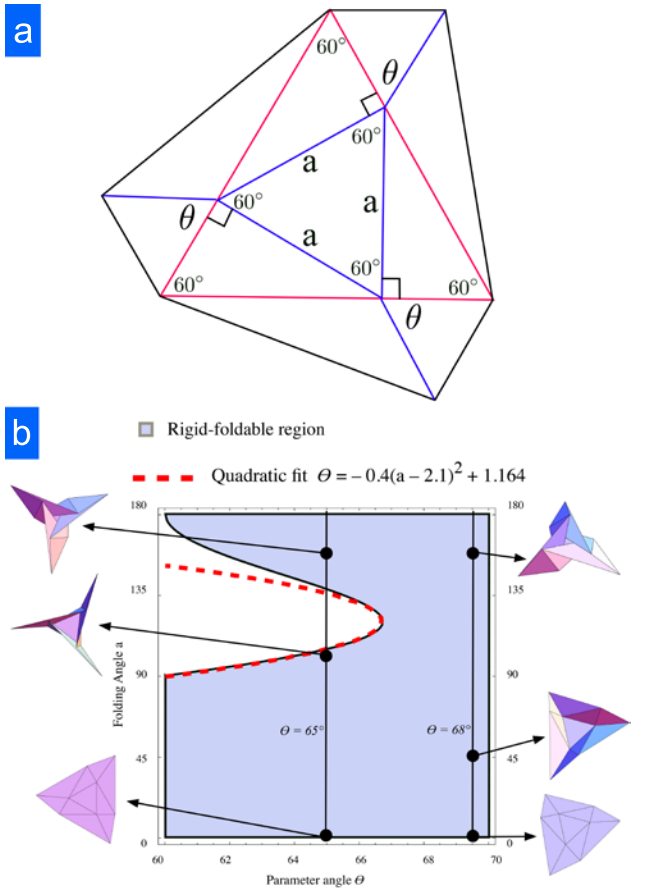

FIG. S7. The triangle twist is another folding pattern that exhibits a geometrically driven bifurcation point. (a) The crease pattern for this triangle twist is parameterized in terms of the plane angle θ and the folding angle a. Red and blue lines are mountain and valley creases, respectively. (b) Solving for the geometrically allowed configuration space reveals a bifurcation in a as a function of θ. Insets show examples of the structure along the indicated folding paths, while the red dashed line highlights the local shape of the bifurcation.

* JLS533@cornell.edu

[1] Tachi, T. Geometric considerations for the design of rigid origami structures. In *Proceedings of the International Association for Shell and Spatial Structures (IASS) Symposium*, vol. 12, 458–460 (2010).

[2] Lang, R. J. *Origami Design Secrets: Mathematical Methods for an Ancient Art* (CRC Press, 2011).

[3] Silverberg, J. L. *et al.* Using origami design principles to fold reprogrammable mechanical metamaterials. *Science* **345**, 647–650 (2014).

[4] Evans, T. A., Lang, R. J., Magleby, S. P. & Howell, L. *Rigidly Foldable Origami Twists* (submitted to ORIGAMI6, in review, 2014).

[5] Landau, L. D. & Lifshitz, E. M. *Landau and Lifshitz Course of Theoretical Physics Volume 7: Theory of Elasticity* (Butterworth Heinemann, New Delhi, 1986), 3 edn.

[6] Na, J.-H. *et al.* Programming reversibly self-folding origami with micropatterned photo-crosslinkable polymer trilayers. *Adv. Mater.* **27**, 79–85 (2015).

[7] T, K. & K, M. $r(\gamma) = i$. In *Origami Science and Art: Proceedings of the Second International Meeting of Origami Science and Scientific Origami* (OSSO02 31-40, 1997).

[8] Belcastro, S.-M. & Hull, T. C. Modelling the folding of paper into three dimensions using affine transformations. *Linear Algebra Appl.* **348**, 273–282 (2002).

DOI: 10.1038/NMAT4232

[9] Abel, Z., Hull, T. C. & Tachi, T. Locked rigid origami with multiple degrees of freedom. In *Origami^6: Proceedings of the Sixth International Meeting of Origami Science, Mathematics, and Education* (submitted to ORIGAMI6, in review, 2014).

TESSELLATICA CODE

Download and run Tessellatica from:

`http://www.langorigami.com/science/computational/tessellatica/tessellatica.php`

to predefine all the appropriate functions/objects/attributes. Using Mathematica 9, the following code calculates energies of the facets, creases, as well as the value of the order parameter x/L.

```
TSquareTwistEnergy[ϕ_, Γ_, L_]:=
Module[{v1, v2, v1rot, v2rot, verts, edges, faces, types, tobj, tobjff,
faspecs, foldangles, α, getverts3d},
v1 = L{1, 1};
v1rot = L{−1, 1};
v2 = L{Sin[ϕ] + Cos[ϕ], Cos[ϕ] − Sin[ϕ]};
v2rot = L{Sin[ϕ] − Cos[ϕ], Cos[ϕ] + Sin[ϕ]};
verts = {{0, 0}, v1, v1 + v1rot, v1rot, v2, v2 + v1, v2 + v1 + v2rot,
v1 + v2rot, v1 + v2rot + v1rot, v1 + v2rot + v1rot − v2, v1 + v1rot − v2,
v1rot − v2, v1rot − v2 − v2rot, v1rot − v2rot, −v2rot, v2 − v2rot};
edges = {{1, 3}, {1, 16}, {2, 5}, {2, 7}, {3, 8}, {3, 10}, {4, 11}, {4, 13},
{1, 14}, {1, 2}, {1, 5}, {1, 15}, {1, 4}, {2, 3}, {2, 8}, {2, 6}, {3, 4},
{3, 11}, {3, 9}, {4, 14}, {4, 12}, {5, 6}, {6, 7}, {7, 8}, {8, 9},
{9, 10}, {10, 11}, {11, 12}, {12, 13}, {13, 14}, {14, 15}, {15, 16}, {16, 5}};
(*definedwithfacefoldsfirst, theninternalcreases, thenboundaries*)
faces = {};
types = {U, U, U, U, U, U, U, U, U, M, V, M, M, M, V, M, M, V, M, V, M, B,
B, B, B, B, B, B, B, B, B, B}; (*MMMM central face*)
tobj = MakeTGraph[verts, edges, faces]//AddTAssigned[types]//AddTPlaneGraph;
Do[
α = i * .45 * π/18.1;
faspecs = {{√2Γ, 0}, {√2Γ, 0}, {2ΓSin[ϕ/2], 0}, {√2Γ, 0},
{2ΓSin[ϕ/2], 0}, {√2Γ, 0}, {2ΓSin[ϕ/2], 0}, {√2Γ, 0},
{2ΓSin[ϕ/2], 0}, {1, −α}, {1, α}, {1, −α}, {1, −α}, {1, −α},
{1, α}, {1, −α}, {1, −α}, {1, α}, {1, −α}, {1, α}, {1, −α}, {∞, 0},
{∞, 0}, {∞, 0}, {∞, 0}, {∞, 0}, {∞, 0}, {∞, 0}, {∞, 0}, {∞, 0},
{∞, 0}, {∞, 0}, {∞, 0}};
foldangles = MakeGraphFoldAngles[tobj, faspecs];
tobjff = FoldGraph3D[tobj, foldangles, StationaryFace → 1];
getverts3d = GetValues[tobjff, {Vertices3D}];
FaceEnergy[[i]] = Sum [faspecs[[j, 1]] * foldangles[[j]]^2, {j, 1, 9}] ;
CreaseEnergy[[i]] = Sum [(foldangles[[j]] − faspecs[[j, 2]])^2, {j, 10, 21}] ;
ShapeList[[i]] = FoldedFormGraphics3D[tobjff]/.OrigamiStyle[];
Folds[[i]] = foldangles;
Deltas[[i]] =
√((getverts3d[[1, 14]] − getverts3d[[1, 8]]).
(getverts3d[[1, 14]] − getverts3d[[1, 8]])); ,
{i, 1, 40}]
]
```